Journal of Structural Geology 31 (2009) 662–673

Contents lists available at ScienceDirect

Journal of Structural Geology

journal homepage: www.elsevier.com/locate/jsg

Geometry, displacement–length scaling, and extensional strain of normal faults on Mars with inferences on mechanical stratigraphy of the Martian crust

Anjani T. Polit [a,1], Richard A. Schultz [a,*], Roger Soliva [b]

[a] Geomechanics–Rock Fracture Group, Department of Geological Sciences and Engineering, Mackay School of Earth Sciences and Engineering, University of Nevada, Reno, NV 89557–0138, United States
[b] Université Montpellier II, Département des Sciences de la Terre et de l'Environnement, 34000 Montpellier, France

ARTICLE INFO

Article history:
Received 6 June 2008
Received in revised form
27 February 2009
Accepted 17 March 2009
Available online 15 April 2009

Keywords:
Displacement–length scaling
Normal faults
Grabens
Mars
Fault restriction

ABSTRACT

We measure throw distributions for graben-bounding normal faults from two areas on Mars to investigate fault growth, displacement–length (D_{max}–L) scaling, and extensional strain using a complementary suite of techniques. Faults in the northern plains are inferred to be restricted at 2–3 km depth, as shown by a transition from linear scaling, with D_{max}–L ratios of $\sim 1 \times 10^{-3}$, to nonlinear scaling for faults >50 km long. On the Alba Patera volcano, faults conform to linear D_{max}–L scaling, with a D_{max}–L ratio of $\sim 6 \times 10^{-3}$, consistent with more deeply penetrating faults that are not restricted at depth. These grabens accommodate larger extensional strains (~0.84%) than the faults in the northern plains (~0.23%), with a temporal change from regionally distributed to localized deformation and associated increases in D_{max}–L ratio, extensional strain, and perhaps down-dip fault height. The results suggest that both spatial and temporal variations in extensional strain and displacement–length scaling relations, along with fault restriction, are recorded by Martian fault populations.

1. Introduction

Fault maximum displacement–length (D_{max}–L) scaling relations and displacement distributions have been studied in recent years to aid in the understanding of fault growth (e.g. Cowie and Scholz, 1992a,b; Dawers et al., 1993; Scholz et al., 1993; Scholz, 1997; Schultz and Fossen, 2002; Soliva and Benedicto, 2005). Although early work advocated $D \propto L^n$, where $1 \leq n \leq 2$, more recent studies have shown a linear relation between D and L, such that $n = 1$ for isolated faults that grow proportionally in length and height (Cowie and Scholz, 1992a,b; Dawers et al., 1993; Villemin et al., 1995; Schlische et al., 1996; Clark and Cox, 1996; Scholz, 2002; Schultz et al., 2006, 2008, in press). The magnitudes and distributions of displacement along a fault are controlled by factors such as fault length, fault shape (aspect ratio, given for buried faults by horizontal length/down-dip height; Willemse et al., 1996; Schultz and Fossen, 2002), mechanical interaction with other faults, segment linkage, far-field stresses, friction, elastic properties of the host rock, and variations in lithology (see Schultz, 1999; Soliva and Schultz, 2008 for reviews). Displacement–length scaling can therefore be a useful tool in evaluating how these parameters affect fault populations throughout their growth history (see review by Schultz et al., in press).

Faults can become vertically restricted by variations in mechanical stratigraphy, such that an interface or adjacent layer inhibits downward propagation of a fault (e.g. Nicol et al., 1996; Gross et al., 1997; Wilkins and Gross, 2002; Benedicto et al., 2003; Soliva and Benedicto, 2005). As the horizontal length of a stratigraphically restricted fault continues to increase (increasing its aspect ratio), the amount of displacement per unit length decreases until the fault's down-dip height controls the displacement magnitude (Willemse et al., 1996; Schultz and Fossen, 2002; Soliva and Benedicto, 2005; Soliva et al., 2005a,b; Soliva and Schultz, 2008). This manifests as a change from linear D_{max}–L scaling (unit slope on D_{max}–L diagram) to nonlinear scaling (shallower trend on D_{max}–L diagram) as shown conceptually in Fig. 1(a) and (b).

In a setting with distributed deformation, vertically restricted faults follow exponential frequency–length scaling (Cowie et al., 1993; Carbotte and Macdonald, 1994; Spyropoulos et al., 1999; Soliva and Schultz, 2008), rather than the power-law scaling

* Corresponding author.
E-mail address: schultz@mines.unr.edu (R.A. Schultz).
[1] Present address: Lunar and Planetary Laboratory, The University of Arizona, Tucson, AZ 85721-0063, United States.

0191-8141/$ – see front matter © 2009 Elsevier Ltd. All rights reserved.
doi:10.1016/j.jsg.2009.03.016

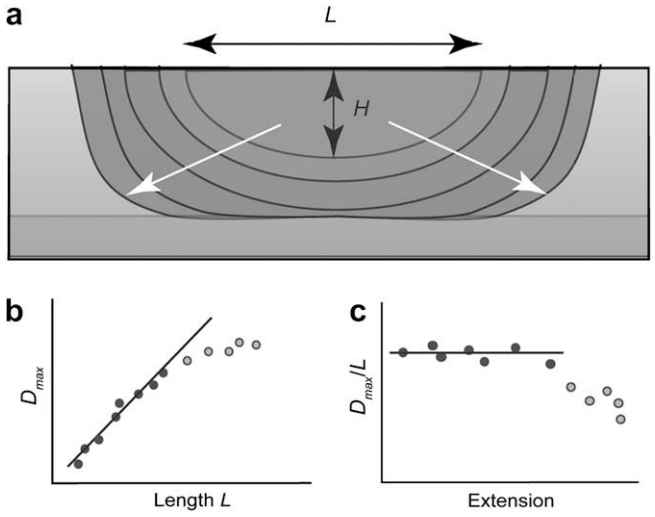

Fig. 1. Conceptual diagrams of fault evolution. (a) Growth from an unrestricted to a restricted fault with increases in length and height manifested as a transition from linear to nonlinear D_{max}–L scaling (b) and a decrease in D_{max}/L ratio (c) with extension or extensional strain.

observed for localized/scale-invariant faulting regimes (Scholz and Cowie, 1990; Scholz et al., 1993; Scholz, 1997; Bohnenstiehl and Kleinrock, 1999; Spyropoulos, et al., 1999; Soliva and Schultz, 2008). The transition from power-law to exponential scaling is thought to occur with increasing extensional strain and when fault density has reached a saturation point (Spyropoulos et al., 1999; Ackermann et al., 2001) or maximum value such that stress shadowing impedes nucleation and propagation of additional faults (Gupta and Scholz, 2000b; Soliva et al., 2006). The extensional strain at which the scaling transition occurs is dependent upon the thickness of the mechanical layer in which the faults are confined (Ackermann et al., 2001). Accompanying the transition in length–frequency scaling is a decrease in the D_{max}–L ratio (Fig. 1(c)) which can occur in association with fault restriction (Ackermann et al., 2001; Soliva et al., 2006). Fault populations can switch between distributed and localized deformation in accordance with whether they are restricted or have broken through mechanical layer boundaries (Ackermann et al., 2001; Soliva et al., 2006; Soliva and Schultz, 2008; Schultz et al., in press).

We present a study of surface-breaking normal faults from two areas on Mars. The graben-bounding faults are well exposed, with minimal erosion and deposition because of the thin Martian atmosphere and little to no surface water. Because D_{max}–L scaling can provide information on factors leading to fault growth and fault population evolution, we use it as the basis for this analysis. We use fault-related topography from data acquired by the Mars Global Surveyor spacecraft to analyze and interpret fault growth, extensional strain, and infer the mechanical stratigraphies of Alba Patera and the northern plains.

2. Study areas

The two study areas are located in the northern part of the Tharsis volcanotectonic province of Mars (Fig. 2(a); Carr, 1974; Plescia and Saunders, 1982). Tharsis is a topographic rise topped by the largest Martian shield volcanoes (Scott and Tanaka, 1986; Phillips et al., 2001; Golombek and Phillips, in press). The formation of Tharsis induced significant magmatism, volcanism, and tectonism, including the radial graben sets (Carr, 1974; Banerdt et al., 1992; Anderson et al., 2001; Knapmeyer et al., 2006) analyzed in this paper. Although Tharsis may have been formed by one or more major mantle plumes during Noachian time (~4 Ga), extruded volcanic material probably accounts for most of the current topography (Solomon and Head, 1982; Mège and Masson, 1996; Zuber et al., 2000; Williams et al., 2008).

The faults studied, shown in Fig. 2(a), are part of the Tantalus Fossae normal fault population continuing northeastward from the large shield volcano Alba Patera into the northern plains. We analyze the distal segments of Tantalus Fossae located in the northern plains (Fig. 2(b)) and faults on the eastern flank of Alba Patera (Fig. 2(c)). The first study area (Fig. 2(b)) is located in the northern plains, a region interpreted to be a sedimentary sequence, of undetermined thickness, eroded from the highland materials that overlies volcanic flows (Frey et al., 2002; Tanaka et al., 2003). The faults in the Alba Patera study area (Fig. 2(c)) cut a sequence of basaltic (Christensen et al., 2000; Hamilton et al., 2001) lava flows, also of undetermined thickness, from the middle member of the Alba Patera Formation (Scott and Tanaka, 1986). Some workers have inferred that grabens in Tharsis are dike related (e.g. Mège and Masson, 1996; Ernst et al., 2001; Cailleau et al., 2005) although none of the grabens we investigated show features consistent with dike-induced graben formation such as pit craters, troughs, or lava flows emanating from the grabens (e.g. Ernst et al., 2001).

Several sequential stages of faulting around Alba Patera were identified by Tanaka (1990), with the faults in this study belonging to his Stage 3. These faults are the youngest except for a few crosscutting features that do not affect the faults we analyzed. The grabens are linear to curved on the flank of Alba Patera and extend to the northeast of the shield volcano. We do not analyze grabens from earlier stages of faulting because they have a more subdued appearance in images and have likely been infilled by younger materials (e.g. Tanaka, 1990) such that they have undergone more erosional modification than the faults we investigate. The studied faults are part of the Stage 4 extensional structures identified by Anderson et al. (2001) that formed in the Late Hesperian-Early Amazonian (with an age of perhaps 3 Ga), making them some of the youngest faults recognized on Mars (see Hartmann and Neukum, 2001 for a summary of the chronology of Mars). Mapping of tectonic activity on Mars by Anderson et al. (2001) and Knapmeyer et al. (2006) suggests that the basic lithospheric structure and stress fields of the Tharsis region have not changed significantly since early Martian history some 4 Ga ago (e.g. Phillips et al., 2001; Williams et al., 2008; Golombek and Phillips, in press).

Faults concentric to Alba Patera formed after the radial grabens that strike to the north–northeast, suggesting a temporal change from a radial to concentric pattern (Cailleau et al., 2003). The pattern of radial grabens was reproduced in modeling studies by combining regional stress with a broad uplift due to a buoyancy zone under Alba Patera (Cailleau et al., 2005). The concentric grabens were reproduced in both numerical and physical models by local crustal subsidence (related to the formation and evolution of Alba Patera) superimposed on a regional extension, with the increasing subsidence causing the predominance of concentric faults in later stages of faulting (Cailleau et al., 2003).

3. Methods

Faults in this paper were identified using Viking Orbiter data (controlled digital photomosaics of the Arcadia Northeast, Northwest, and Southwest quadrangles, with resolution of ~256 pixels/°) and high-resolution digital elevation models (DEMs) from Mars Global Surveyor. We use DEMs gridded at 200 pixels/°, based on Mars Orbiter Laser Altimeter (MOLA) data (Smith et al., 2001; Okubo et al., 2004), to measure the throw as a function of fault length (also measured by using MOLA data) for graben-bounding normal faults on Mars. Crossover-corrected MOLA data have

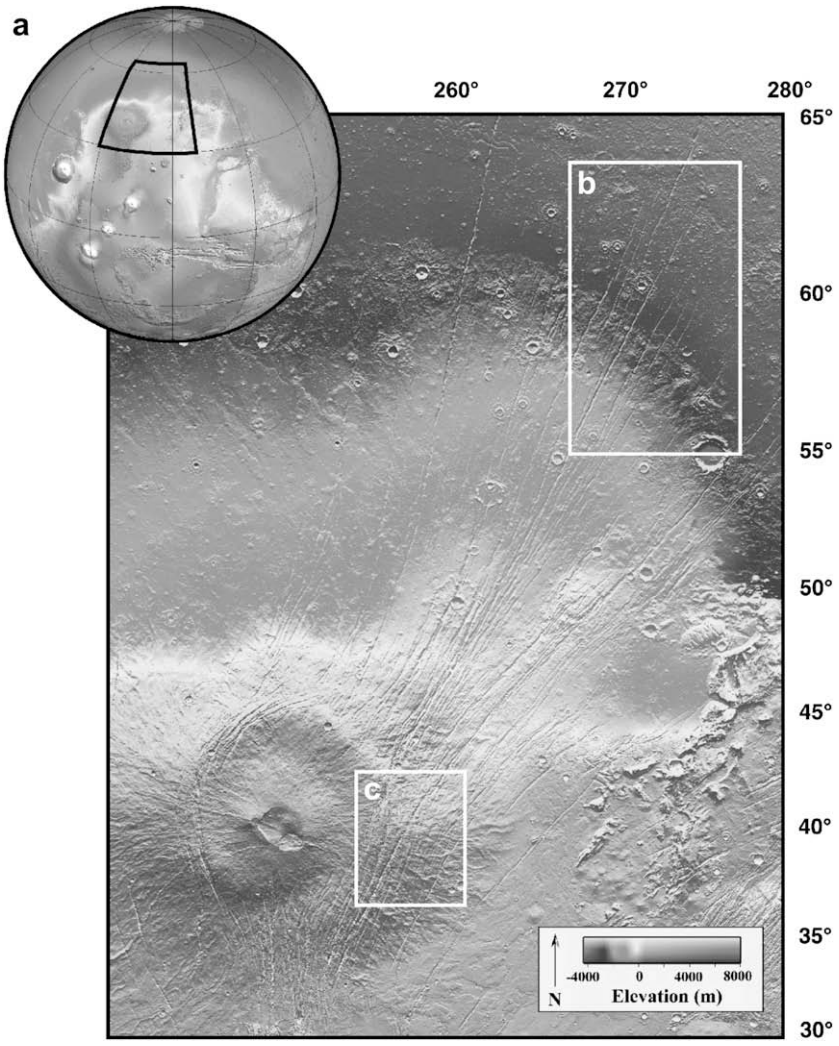

Fig. 2. Mars Orbiter Laser Altimeter (MOLA) shaded relief digital elevation models (DEMs) of the study areas. Coordinates are given in latitude and east longitude following conventions for Mars used by the Mars Global Surveyor (MGS) spacecraft team. (a) Northern plains and Alba Patera study areas are outlined. (b) Grabens in the northern plains are traced in white and numbered for reference. (c) The faults studied on Alba Patera are traced in black. Inset boxes show locations of Fig. 5(a) and (b). Note changes in elevation scales.

vertical precision typically less than 1 m, with a surface spot size of ~168 m and shot-to-shot spacing on the Martian surface of ~300 m (Smith et al., 2001). In the northern plains study area we use near-neighbor gridding (Okubo et al., 2004) because of the relatively small fault displacement magnitude and high data density. On Alba Patera, there is lower data density and data lines are almost parallel to the fault strikes, making use of near-neighbor DEMs impractical. On Alba Patera we utilize a surface-interpolated DEM that has uncertainties that are comparable to the uncertainty of the original MOLA data (Okubo et al., 2004). MOLA topography currently provides the best dataset for this type of study in extracting fault topography over the large regions of interest on Mars.

We use cross-sectional topographic profiles extrapolated from the DEMs by use of IDL-based Gridview (e.g. Roark and Frey, 2001) to measure scarp height for each graben-bounding fault (e.g. Fig. 3). Care was taken to measure the maximum vertical relief, which corresponds to a minimum magnitude of fault throw because of the possibility of erosion in fault footwalls and deposition of materials on the hanging walls. The surface of Mars in the fault footwalls is in some locations quite rough compared to the scale of the fault throws making exact throw measurements difficult. For most measurements in the northern plains, we estimated fault throw errors of ±3 m. On Alba Patera the estimate of fault throw errors is ±5 m. For most measurements the error bars are contained within the symbols in the throw distribution diagrams and the estimated uncertainties for throw measurements exceed the uncertainties in the topographic data.

To evaluate erosion of fault scarps and graben infilling, we conducted a qualitative comparison between faults from both study areas. We analyzed high-resolution data from the Thermal Emission Imaging System (THEMIS), including infrared (100 m/pixel resolution) and visible (19 m/pixel resolution) images, and images from the Mars Orbiter Camera between ~1.5 m/pixel and ~12 m/pixel to note general graben character. Using these data we constructed cross-strike profiles of grabens with similar throws and width and measured graben wall slopes, noted whether the grabens have distinct or sediment-covered floors, and took elevation data for graben plateaus and floors to identify obvious infilling. The grabens on Alba Patera are more pristine with greater wall slopes and a crisp appearance in imagery, while those in the northern plains are more subdued and less distinct in imagery as shown in Fig. 4. The observations confirm differences in the physical properties of faulted materials in the two study areas since the faults in both areas are considered to be the same age (e.g. Anderson et al., 2001). We also do not observe a flattening of graben

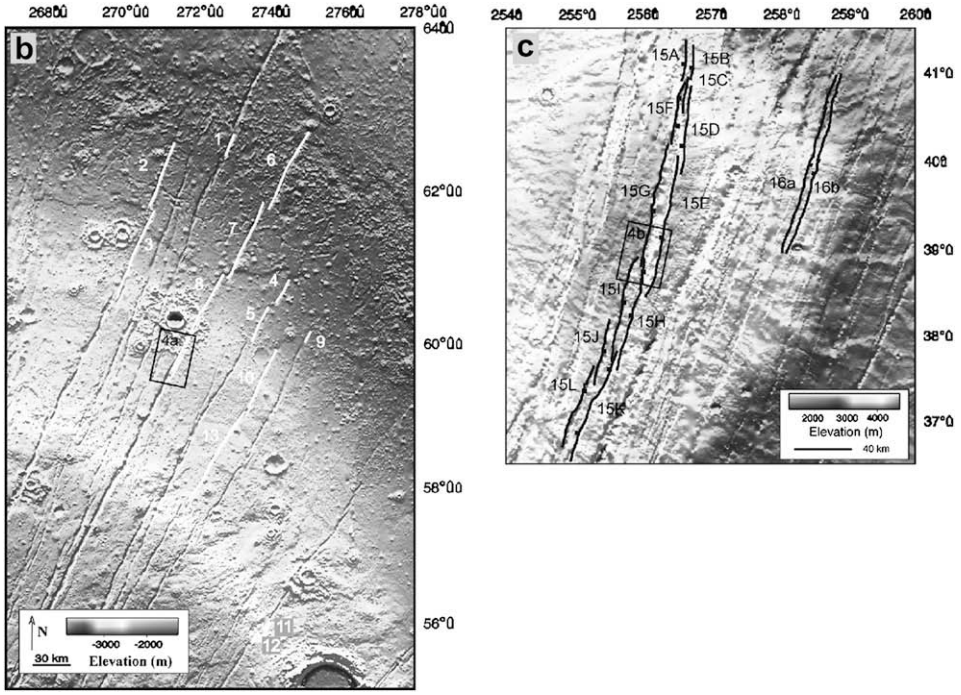

Fig. 2. (*continued*).

floors that might be expected if significant graben infilling has occurred, suggesting that there is not significantly more infilling in the northern plains than on Alba Patera. From the data examined, the throw profiles appear to be reliable records of the structural topography.

To construct throw distributions and D_{max}–L diagrams, fault length needs to be correctly and consistently identified. Many grabens occur in echelon patterns in which fault interaction occurs. Faults in close proximity to each other mechanically interact through their stress fields, impeding or promoting fault growth along strike and increasing displacement gradients at fault ends compared to an ideal non-interacting ("isolated") fault profile (e.g. Peacock, 1991; Peacock and Sanderson, 1991, 1994; Willemse et al., 1996; Willemse, 1997; Crider and Pollard, 1998; Gupta and Scholz, 2000a; Kattenhorn and Pollard, 2001). Faults are considered to be soft-linked when they are mechanically interacting but not physically bridged by a connecting fault. Hard linkage refers to faults that are physically linked. In this study faults that are soft-linked are considered to be separate faults, with the acknowledgement that they may be physically linked in the subsurface (e.g. Soliva et al., 2008). We identify fault terminations (location along the fault where displacement equals zero) within the resolution of the data.

The two-dimensional displacement-discontinuity boundary element model FAULT (Schultz and Aydin, 1990; Schultz, 1992) was used to calculate the displacement profile of the Martian surface above a surface-breaking fault for comparison with the MOLA-based cross-strike topography of Martian grabens to quantify the depth of faulting and fault dip (see Schultz and Lin, 2001). FAULT uses standard displacement-discontinuity equations (Crouch, 1976; Crouch and Starfield, 1983) to find the fault displacement values that are consistent with the fault's constitutive relations (i.e., frictional strength) and prescribed remote (tectonic) stresses. Forward mechanical models are used to calculate the displacements of the Martian surface resulting from the fault displacements. Using the program's elastic half-space solution, we specify the gravitational acceleration, rock density, physical fault characteristics (down-dip fault height, fault dip angle, friction coefficient), rock mass stiffness (Poisson's ratio, Young's modulus), and the driving stress (expressed through the remote tectonic principal-stress ratio). This two-dimensional modeling approach, when applied to a vertical, cross-sectional slice through a graben as done in this paper (see also Schultz and Lin, 2001; Okubo and Schultz, 2004 for comparable applications), provides information on the third (i.e., depth) dimension of the faults which is used, in turn, in the analysis of displacement–length scaling relations.

The surface gravity of Mars is 3.7 m/s^2, so that with comparable rock densities (2600 kg/m^3), vertical overburden stress will be 38% of Earth's (e.g. Schultz et al., 2006). We systematically varied all the input parameters in FAULT before identifying values of Young's modulus (15 GPa), Poisson's ratio (0.25), and vertical to horizontal stress ratio (3), fault friction coefficient (iteratively found to be 0.62 for this set of parameters), fault dip, and fault depth to produce

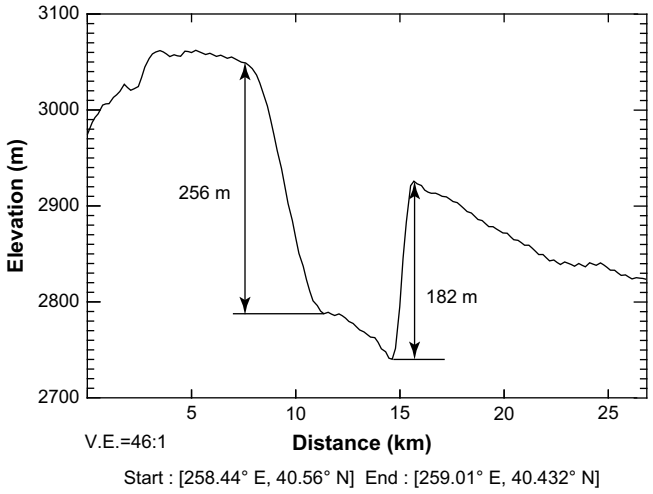

Fig. 3. Cross-sectional topography of Alba Patera graben 16 (see Fig. 2(c)), with throw measurements shown.

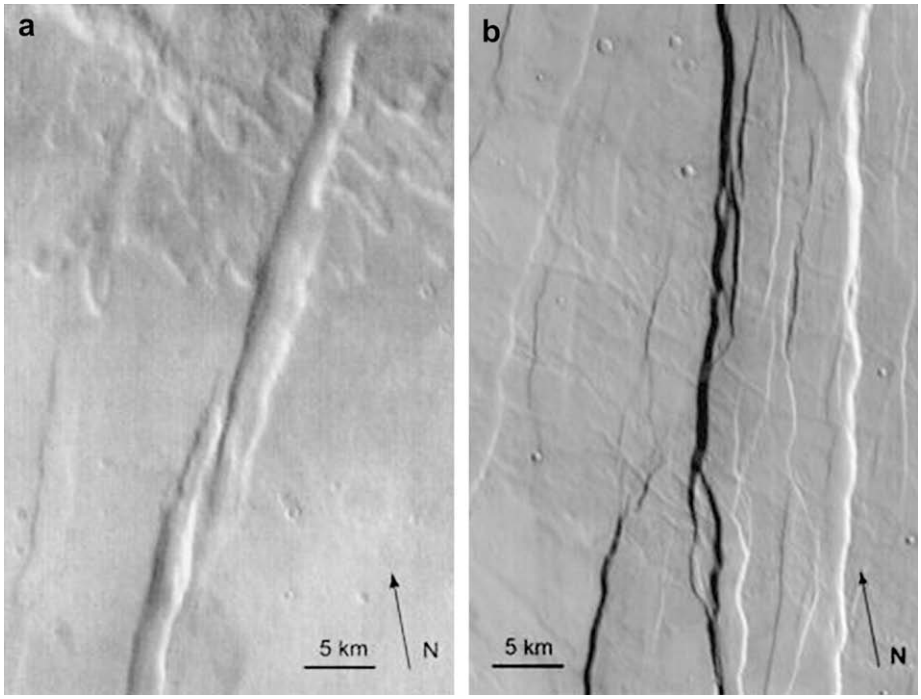

Fig. 4. Two overlapping (soft-linked) grabens in the northern plains (a) (box, Fig. 2(b)) are less distinct in this day infrared THEMIS image than the faults in the THEMIS image of the Alba Patera study area (b) (box, Fig. 2(c)). In northern part of (a), impact ejecta contributes to surface roughness. Faults shown in (b) cut lava flows emanating from Alba Patera. THEMIS images are available at http://themis.asu.edu.

acceptable fits to the cross-strike graben topography (i.e., ±10% of MOLA elevations; see Schultz and Lin, 2001 and Okubo and Schultz, 2004 for discussions of parameter sensitivity and variations). A Young's modulus of 15 GPa is consistent with typical values for terrestrial and Martian rock masses (Schultz, 1995, 1996; Schultz et al., 2006).

To investigate D_{max}–L scaling of the Martian normal faults, we utilize the analytical solution for three-dimensional fault scaling developed by Schultz and Fossen (2002) and applied to fault systems on Earth and Mars by Soliva et al. (2005a,b), Schultz et al. (2006) and Soliva and Schultz (2008). Following Schultz and Fossen (2002) and Schultz et al. (2006) the displacement–length relationship for a fault with horizontal length $L = 2a$ and down-dip height $H = 2b$ is given by

$$\frac{D_{max}}{L} = \frac{2(1-\nu^2)}{E} \frac{\left\{\sigma_d - \sigma_y\left[1 - \cos\left(\frac{\pi\sigma_d}{2\sigma_y}\right)\right]\right\}}{\sqrt{1 + 1.464\left(\frac{a}{b}\right)^{1.65}}} \quad (1)$$

where ν is Poisson's ratio, E is Young's modulus, σ_d is the cumulative driving stress (integrated over the life-time of the fault: Cowie and Scholz, 1992b; Gupta and Scholz, 2000a; Schultz, 2003) on the fault, and σ_y is the yield strength of the surrounding rock at the fault tip (variables given in Table 1). This formulation assumes that we are examining the D_{max}/L profile in the horizontal plane (i.e., $L = 2a$) such that θ, which denotes the position around the fault tipline as defined by Schultz and Fossen (2002), is zero. Employing this model of D_{max}–L scaling (through use of a spreadsheet) we vary parameters to achieve an acceptable fit with the measured fault throws (±10% of the MOLA elevations), as converted into fault displacements by using appropriate dip angles for the faults.

Fault heights obtained from the FAULT modeling ($H = b$ in this case because the faults cut a free surface) are then used as inputs in the D_{max}–L scaling spreadsheet (Schultz and Fossen, 2002; Soliva et al., 2005a,b) in order to test the possible influence of constant down-dip fault height (in the vertical, third dimension) on the D_{max}–L scaling relations observed. Fault shape, taken normal to the fault plane (e.g. Nicol et al., 1996), is parameterized by aspect ratio, AR = L/H, for buried faults, so that a circular fault with $L = H = 2a = 2b = 1$ km, for example, would have AR = 1.0. The shape of a surface-breaking fault is parameterized here by its length ratio, defined in this paper, as LR = $0.5L/H$, so that a semicircular surface fault with $a = b = H = 1$ km and $L = 2a = 2$ km would have LR = 2.0; both faults in these examples have the same map lengths and depths of faulting but are implemented in the D_{max}–L scaling spreadsheet and Eq. (1) by specifying AR or LR as appropriate for blind or surface-breaking faults, respectively.

The horizontal normal (extensional) strains accommodated by faults in the northern plains and on Alba Patera are calculated from fault-normal traverses and fault-related topography from the DEMs (Fig. 5). The horizontal extensional strain normal to fault strike is given by the sum of the heaves (horizontal component of displacement), assuming 60-degree fault dips (consistent with

Table 1
Main variables and parameters used in D_{max}–L calculations.

Section	Symbol	Explanation and units
	D_{max}	Maximum displacement (structural offset) along fault plane, m
	L	Horizontal fault length, m
	H	Fault height measured in fault plane, m
	γ	Ratio of D_{max}/L
	n	Exponent of displacement–length scaling law
	E	Young's modulus of rock surrounding the fault, GPa
	ν	Poisson's ratio of rock surrounding the fault
	σ_d	Shear driving stress on fault, MPa
	σ_y	Shear yield strength of rock mass at the fault tip, MPa
	AR	Fault aspect ratio for buried faults, L/H
	LR	Fault length ratio for surface-breaking faults, $0.5L/H$
	a	Half-length of fault, m
	b	Height of surface-breaking fault, m

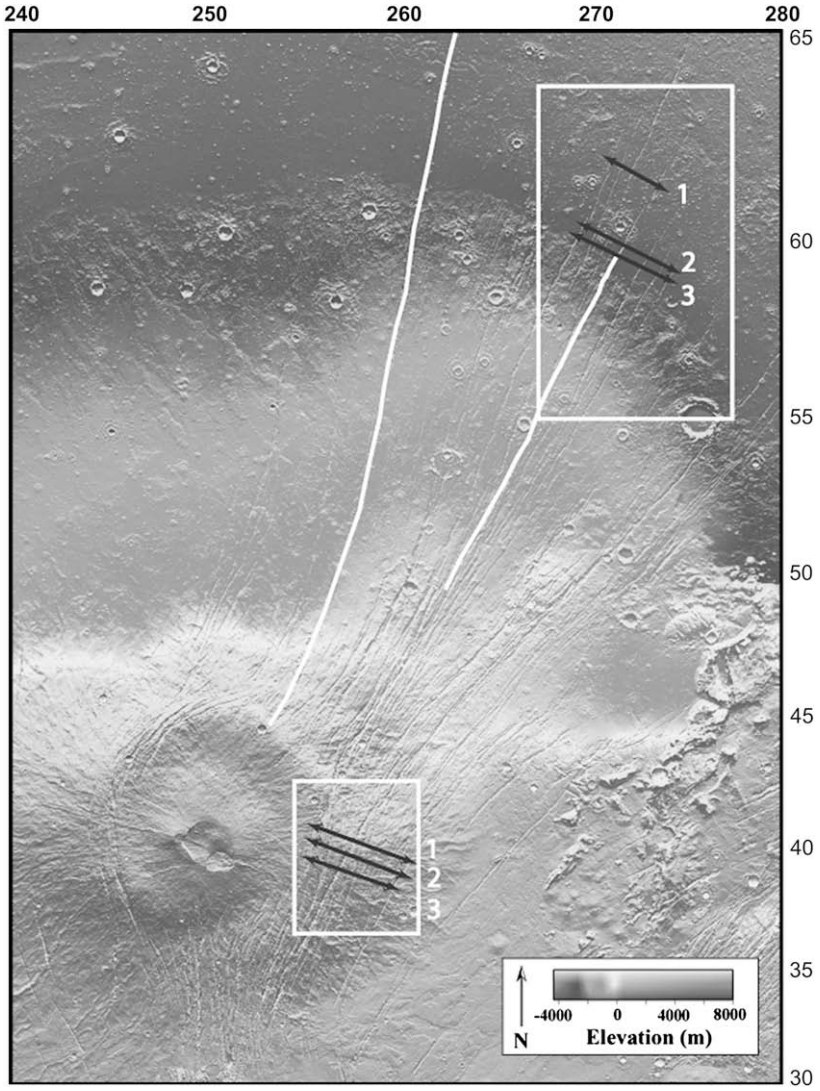

Fig. 5. Traverse locations for extensional strain measurements are shown superimposed on a MOLA DEM of the study areas.

boundary element modeling), along the traverse divided by its original length, defined as traverse length minus the sum of the heaves.

4. Results

We measured throw distributions for 13 grabens that are part of the distal segments of Tantalus Fossae in the northern plains (Fig. 2(b)). Each graben-bounding fault is considered as a separate fault in these analyses. On the eastern flank of Alba Patera (Fig. 2(c)) we identify two distinct domains of deformation. In the east, grabens are more nearly symmetric in terms of graben-bounding fault throws, with approximately regular spacing between grabens. In the west, several faults with substantially larger throws form coalesced grabens that are concentric to Alba Patera.

Fault interaction and linkage effects are identified in the throw distributions of the faults in the northern plains and on Alba Patera. The same characteristics of throw minima at fault tips and maxima

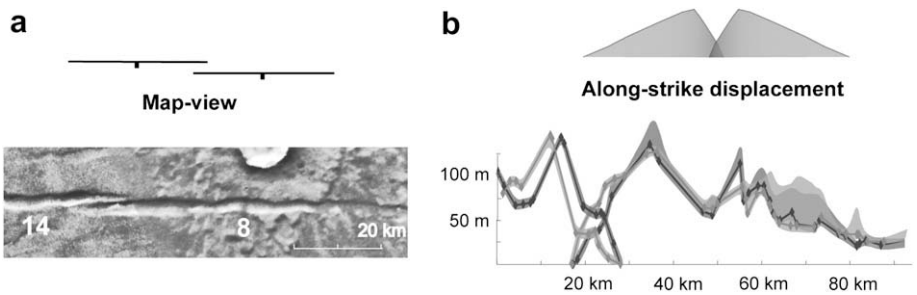

Fig. 6. Fault segments identified in (a) images and (b) throw distributions of northern plains grabens 14 and 8 as asymmetric throw distributions, throw minima at fault segment and graben tips, and large values of throw adjacent to the stepover. Insets show schematic illustrations of map-view fault geometry and along-strike displacement (or throw) distributions for closely spaced echelon normal faults.

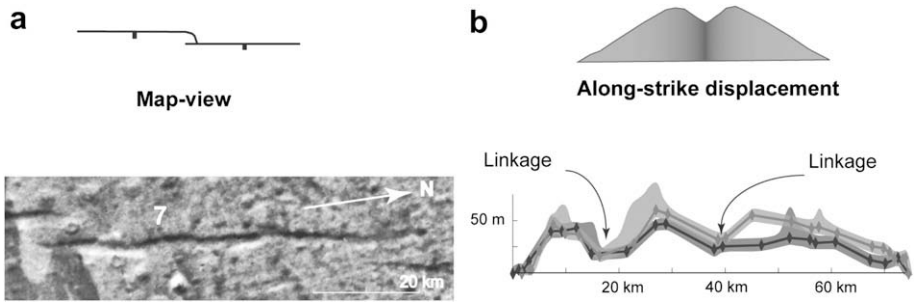

Fig. 7. After physical linkage of Martian faults, the linkage sites are still visible as (a) abandoned fault splays, or abandoned (inactive) fault tips in an image and (b) local displacement minima. Shaded areas indicate uncertainties due to pre-faulting topography.

near fault segment midpoints that are well known on Earth (e.g. Peacock and Sanderson, 1991, 1994; Cartwright et al., 1995; Dawers and Anders, 1995; Willemse et al., 1996; Davies et al., 1997; Willemse, 1997; Gupta and Scholz, 2000a; Soliva and Benedicto, 2004; Soliva et al., 2008) are clearly apparent for the Martian faults. As seen in Fig. 6, throw distributions for faults that overlap and have short separation distances from other faults in map-view (i.e., soft-linked or echelon faults) have skewed/asymmetric throw distributions. In addition, as shown in Fig. 7, local displacement minima can be identified in throw distributions that correspond to sites of fault linkage. In Fig. 7 an abandoned fault splay can be identified at a local displacement minimum. Plateaued throw distributions along grabens in the northern plains (Fig. 8) are suggestive of restriction of the faults at depth (e.g. Soliva et al., 2005a,b).

4.1. Northern plains study area

Normalized throw distributions for the distal segments of Tantalus Fossae (Fig. 2(b)) are shown in Fig. 9(a). Many of the throw distributions resemble the peaked ones found by Dawers et al. (1993) and Soliva et al. (2005a,b) to be associated with spatially isolated, unrestricted, minimally interacting faults. Other, longer faults in this study area show smaller values of normalized throw with more plateau-like throw distributions that resemble those of stratigraphically restricted faults (e.g. Soliva et al., 2005a,b). The results discussed here and compiled in Table 2 are consistent with normal faults in the northern plains study area that are not restricted at depth for lengths $<$50 km and restricted at depth at greater lengths.

Using FAULT, we calculated fault-related topography and then iteratively matched the cross-strike topography of the measured faults. We used three cross-strike profiles taken from different locations along graben 13 in the northern plains (see Fig. 2(b)). Fits are shown in Fig. 10 with the MOLA topography and best-fit output from the modeling program superimposed. Fault heights range from 2.6 to 3.35 km, with fault dip angles between 55° and 65°. Although transect 3 is somewhat close to a fault tip, it is in the plateau-like section of the displacement profile (not affected by the near-tip region) and therefore can be approximated with a two-dimensional model. Furthermore, the results of the FAULT modeling show no substantive difference between the three transects.

4.2. Alba Patera study area

Normalized throw distributions for the faults on Alba Patera (Fig. 2(c)) are shown in Fig. 9(b). Normal faults in the western part of the study area show peaked distributions, whereas those in the eastern part exhibit plateaued distributions. However, in contrast to the northern plains study area, faults in the Alba Patera study area do not show a consistent change from peaked to plateaued throw distributions with increasing length, perhaps due to the limited range of fault lengths available there, but instead show a geographic change with peaked throw distributions in the western part of the study area and plateaued ones in the east.

We produced best fits to a cross-strike profile through faults 15E and 15G (bounding faults of a large coalesced graben in the western part of the study area) and to a profile through a smaller narrow graben in the eastern part of the study area (#16) using FAULT to evaluate fault dip and depth as shown in Fig. 11. The fit for fault E has a 15.2 km down-dip fault height with a dip of 55°, while a fit for fault G has a fault height of 15.1 km, also with a dip of 55°. The cross-strike separation between the two faults at the surface is 11.5 km. In contrast, the shallower and narrower eastern graben is fit by fault heights of 6.75 km with a dip of 60° and width at the surface between the graben-bounding faults of 6.5 km.

4.3. Strain measurements

We calculate values of normal (extensional) strain to compare the northern plains study area to that closer to the center of Tharsis on Alba Patera. Within the northern plains study area, extensional normal strain increases from north to south (see Table 3). The northernmost traverse (see Fig. 5 for location) crosses the fewest number of faults and has an extensional strain of 0.19%. The southernmost traverse crosses additional faults that are located just south of the study area, so the increase in extensional strain from north to south incorporates the displacements of those faults. Extensional strains range from 0.19 to 0.27% with the average extensional strain for the three traverses being 0.23%.

On Alba Patera the average extensional strain is several times larger than the extensional strain in the northern plains (Table 3). The largest extensional strain (0.94%) is for the northernmost traverse, while the least amount of extensional strain is for the southernmost traverse (0.76%). Average extensional strain from the three traverses is 0.84%.

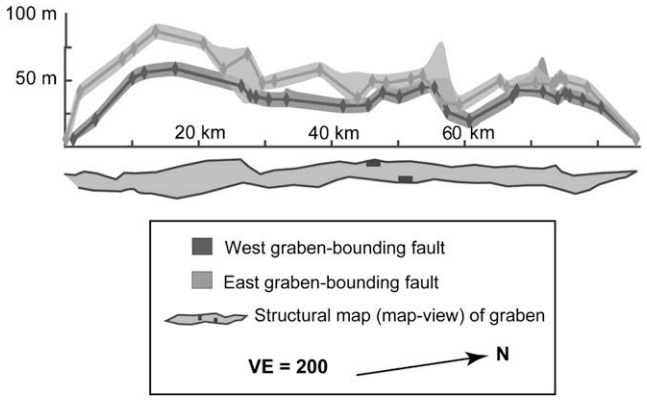

Fig. 8. Throw values for northern plains graben 3 (Fig. 2(b)) showing non-peaked, plateaued distribution.

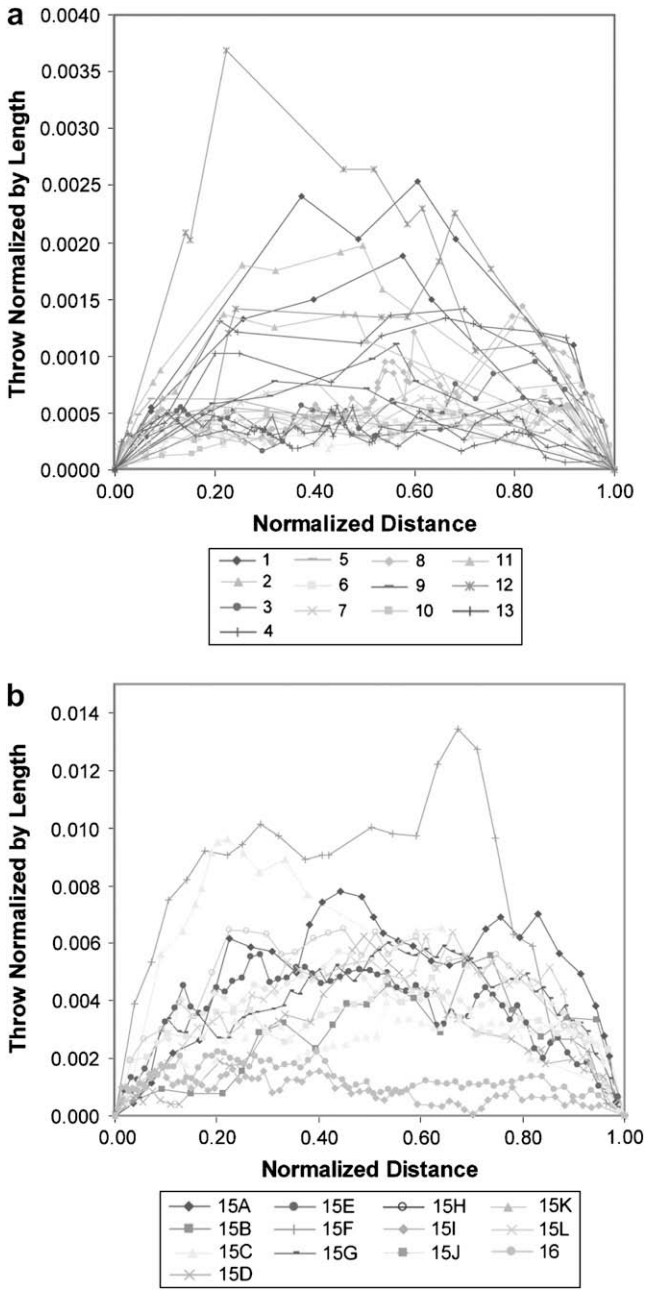

Fig. 9. Throw distributions normalized by fault length. (a) Northern plains grabens (key lists graben numbers shown in Fig. 2(b)). Peaked distributions occur for shorter grabens whereas more plateaued distributions are found for longer grabens. (b) Normalized throw distributions for Alba Patera faults (key lists graben numbers shown in Fig. 2(c)). Graben 16 (in the eastern part of the study area) with a plateaued distribution plots at the bottom, separately from the other faults from the western part of the study area that have more peaked distributions.

In accordance with the observed differences in fault characteristics (i.e., throw, graben spacing) between the eastern and western parts of the Alba Patera study area, we also separately calculate the extensional strains in those domains. For each traverse we iteratively evaluated the cutoff between east and west based upon the DEM map-view of the faults and upon the cross-strike topography. We observe a difference between distributed deformation to the east and localized deformation (expressed as wider and deeper grabens that accommodate more extensional strain) to the west (e.g. see analogous relationships in the Afar region of Africa identified by Soliva and Schultz, 2008). The average extensional strain for the western (localized strain) region is 1.13%, while the average extensional strain for the eastern (distributed strain) region is 0.83%, as listed in Table 3 (see also Polit, 2005). These extensional strain values demonstrate differences in fault population character between the eastern and western parts of the Alba Patera study area that were not identified in previous studies.

Table 2
Dimensions of selected Martian grabens.

Study area[a]	Fault[b]	Length L, km	D_{max}, m	D_{max}/L	Profile shape
NP	9a1	11.9	13.9	0.00117	Peaked
	9b1	19.4	19.6	0.00101	Peaked
	4a1	27.8	30.0	0.00108	Peaked
	4b1	29.8	32.3	0.00109	Peaked
	2a1	54.2	46.2	0.000852	Plateau
	10b1	92.0	45.0	0.000490	Plateau
	6a1	105.0	40.4	0.000385	Plateau
	6b1	112.2	50.8	0.000453	Plateau
	10a1	131.1	46.2	0.000352	Plateau
AW	15A1	36.15	347.6	0.00961	Peaked
	15B1	42.77	177.8	0.00416	Peaked
	15J2	47.05	329.1	0.00700	Peaked
	15H2	71.44	497.7	0.00697	Peaked
	15J1	76.11	329.1	0.00432	Peaked
	15I1	79.64	584.3	0.00734	Peaked
	15L1	94.07	511.5	0.00544	Peaked
	15G1	126.4	809.5	0.00641	Peaked
	15E1	161.2	707.8	0.00439	Peaked
AE	16A	143.1	370.7	0.0026	Plateau
	16B	143.4	296.8	0.0021	Plateau

[a] NP, Northern plains study area; AW, Alba Patera study area (western part); AE, Alba Patera study area (eastern part).
[b] a, western graben-bounding fault; b, eastern graben-bounding fault; 1, northern half of graben-bounding fault; 2, southern half of graben-bounding fault; A–L, graben segment (Fig. 2c).

5. Discussion and implications

5.1. Displacement–length scaling

Identification of graben segmentation and abandoned splays on faults (see examples in Figs. 6 and 7) shows that faults from both study areas of Mars grow by segment linkage along strike, like many faults on Earth (e.g. Cartwright et al., 1995). The northern plains grabens typically show subequal throws on the graben-bounding fault pairs, with grabens in the eastern part of the Alba Patera study area exhibiting a similar character. The grabens in the western part of the Alba Patera study area are part of a larger coalesced graben structure that differs in scale and morphology from the smaller grabens to the east and those in the northern plains study area. This difference is also reflected in the larger extensional strains accommodated by these faults relative to those in the northern plains.

The displacement–length scaling relations for the non-interacting, isolated Martian faults are shown in Fig. 12 (see Table 2). Faults in the northern plains study area are consistent with linear D_{max}–L scaling, with $\gamma \sim 10^{-3}$, for lengths <50 km (Fig. 12(a)). These faults are characterized by peaked displacement distributions. At greater lengths, the fault lengths and offsets are consistent with three-dimensional scaling relations with depths of faulting between 2 and 3 km (curves on Fig. 12(a)), assuming $\sigma_d = 100$ MPa, $\sigma_y = 180$ MPa, $\nu = 0.25$, and $E = 10$ GPa, consistent with values for sedimentary rocks; these faults also exhibit plateaued displacement distributions. The northern plains faults <50 km long are fitted by length ratios of $L/H = 4$, comparable to aspect ratios of blind terrestrial faults (Nicol et al., 1996).

The value of Young's modulus E used in the displacement–length analysis, 10 GPa, differs from that assumed in the FAULT calculations ($E = 15$ GPa). The reason for this is that the FAULT solution assumes

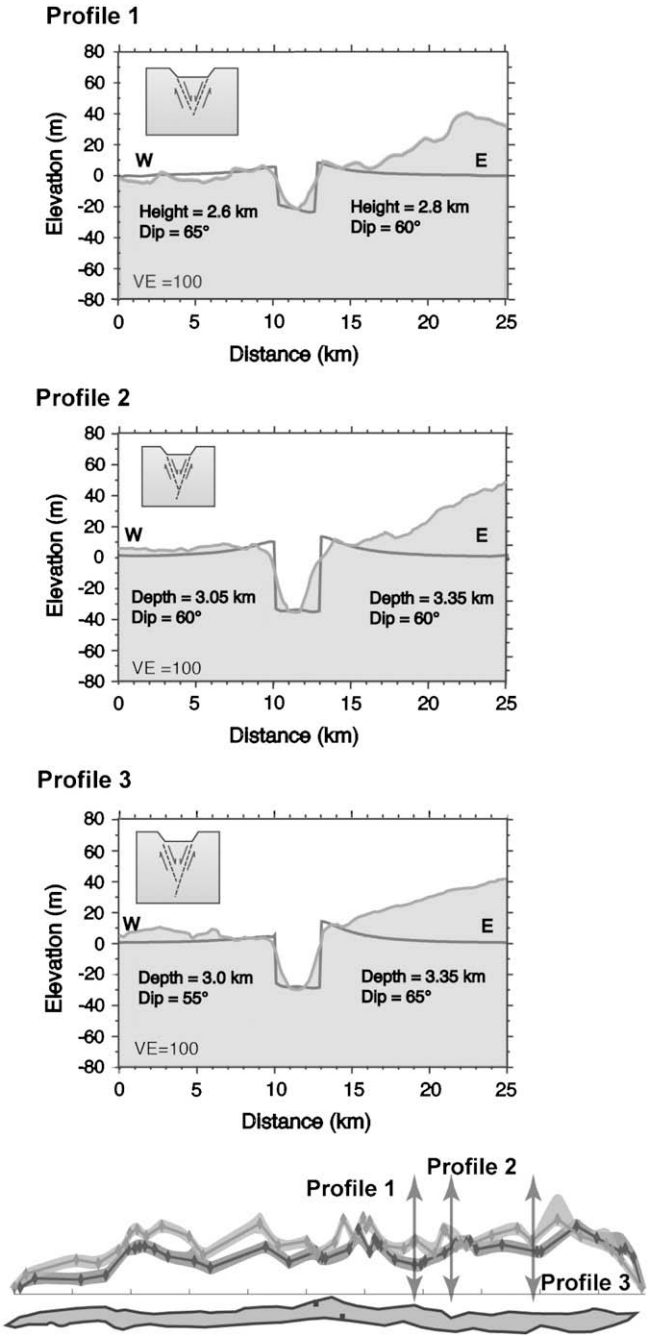

Fig. 10. FAULT fits (smooth curve) and MOLA cross-strike topography (shaded) shown for three profiles from northern plains graben 13 having a total length of 100 km. Fault dips range from 55° to 65°, with fault depths between 2.6 km and 3.35 km. Insets show resulting graben geometries (Vertical exaggeration VE = 1).

an elastic half-space, appropriate to surface-breaking faults such as those investigated in this study, whereas the displacement–length equations assume an elastic full-space (Schultz and Fossen, 2002). Once a value of Young's modulus is chosen in FAULT's half-space solution, fault displacements are calculated and compared to MOLA topography, with values of driving stress that are modified in the half-space solution procedure (e.g. Crouch and Starfield, 1983, pp. 164–171; see also Martel, 2004). The magnitude of this effect can be estimated in part by noting that, for faults, D_{max}/L is proportional to σ_d/E, so that a reduction in E from 15 GPa (in the FAULT solution) to 10 GPa (in the displacement–length scaling solution), assuming constant fault height in both cases, implies a corresponding

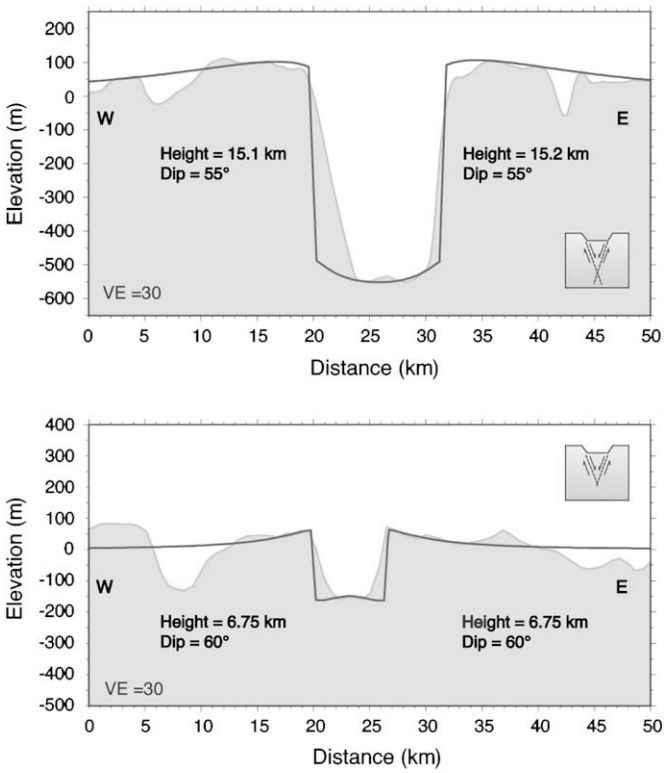

Fig. 11. FAULT fits (smooth curve) and cross-strike topography (shaded) for graben 15 in (upper panel) the western part of the Alba Patera study area (Fig. 2(c)) and (lower panel) for graben 16 in the eastern part. Insets show resulting graben geometries. Note the large differences in fault throw and depth between these two cross-strike profiles. Vertical exaggeration (VE) is 30 for both panels.

reduction in cumulative driving stress σ_d to maintain the same amount of fault offset as given by the MOLA topography. The difference between the two solutions may also be related to variations in modulus and/or yield strength across a heterogeneous (restricting) stratigraphic sequence. We infer from these results that northern plains faults grew initially as unrestricted structures, with proportional increases in length and height, until fault lengths exceeded ~50 km.

The transition from linear to nonlinear D_{max}–L scaling in the northern plains study area is consistent with the longer faults ($L > 50$ km) being vertically restricted. With fault height held constant by a change in layer properties such as modulus or rheology, the aspect or length ratio increases with increasing fault length (Willemse et al., 1996; Schultz and Fossen, 2002; Soliva et al., 2005a,b). The resulting change in length ratio is consistent with the decrease in the D_{max}–L ratio that is observed for the northern plains faults (see Fig. 12(a)).

In contrast to the faults in the northern plains study area, those in the Alba Patera study area that have peaked displacement distributions are broadly consistent with linear D_{max}–L scaling, with γ between 5×10^{-3} and 1×10^{-2} (Fig. 12(a)). We infer that these faults are not restricted at depth. However, the narrow graben

Table 3
Extensional strains for Martian grabens.

	Northern plains	Alba Patera	Alba west	Alba east
Traverse 1	0.19%	0.94%	1.14%	1.02%
Traverse 2	0.23%	0.81%	1.16%	1.04%
Traverse 3	0.27%	0.76%	1.08%	0.42%
Average	0.23%	0.84%	1.13%	0.83%

Percentage extensional strain in the northern plains study area and on Alba Patera, with Alba Patera further divided into east and west.

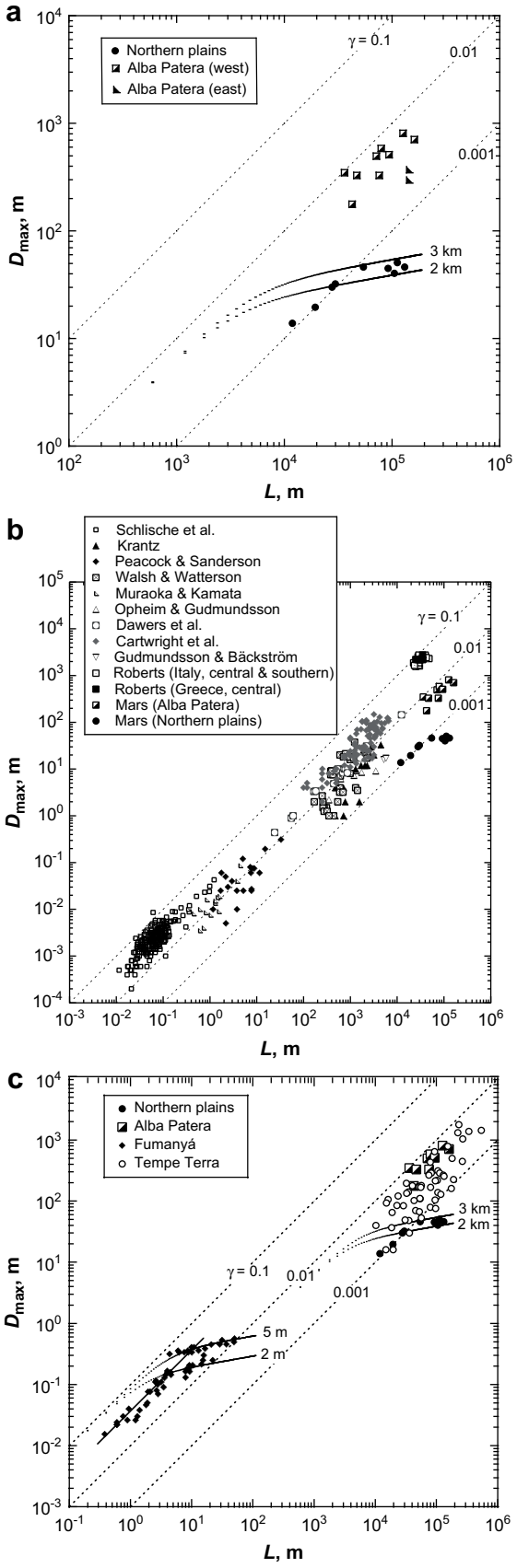

(#16) that we evaluated in the eastern part of the study area is characterized by a plateaued displacement distribution, shallower depth of faulting (~7 km) than the faults in the western part of the study area (15 km; see Fig. 12, solid triangles), and a generally regular spacing with nearby grabens. This graben is consistent with vertical restriction at a depth (~7 km) several times deeper than that inferred for the regularly spaced grabens in the northern plains study area (2–3 km).

The normal faults from both Martian study areas are generally consistent in their scaling with terrestrial normal faults (Fig. 12(b)) and with previous measurements of graben-bounding normal faults from the Tempe Terra region of Mars (Wilkins et al., 2002; Schultz et al., 2006; Fig. 12(c)). Three-dimensional displacement–length scaling of the faults in the northern plains study area is also comparable to the smaller-scale example of stratigraphically restricted normal faults from the eastern Pyrenees documented and analyzed by Soliva et al. (2005a,b).

5.2. Strain magnitudes

The smaller extensional strain magnitudes in the northern plains study area (Table 3) correlate with the smaller D_{max}–L ratios from faults >50 km long in that area (Fig. 12(a)), as noted for terrestrial fault sets by Gupta and Scholz (2000b) and Poulimenos (2000). This relationship is also consistent with the inference that northern plains faults may be vertically restricted to a layer 2–3 km thick (see Soliva and Schultz, 2008, for similar comparisons with terrestrial fault systems). Extensional strain magnitudes increase from the northern plains south along the Tantalus Fossae grabens onto Alba Patera. The increase in extensional strain magnitude to the south is consistent with the independent modeling studies done by Cailleau et al. (2003, 2005), who found that a regional extension increasing towards the south contributed to the formation of the pattern of faulting around Alba Patera and into the northern plains. Using measurements of fault throw, our study demonstrates a general southward increase in extensional strain in this part of Tharsis.

The grabens in the eastern part of the Alba Patera study area accommodate less horizontal extensional strain than those in the western part, and more extensional strain than the faults in the northern plains study area. Correspondingly, the D_{max}–L ratios for faults in the eastern part of the Alba Patera study area are intermediate between those for faults in the western part and those in the northern plains study area. The grabens in the eastern part of the Alba Patera study are similar to those in the northern plains study area in that both fault populations appear to have regular spacings, plateaued displacement distributions, and symmetric throws across the grabens. These characteristics are consistent with restriction of these faults on Alba Patera at ~7 km depth (Fig. 11(lower panel)).

The differences in extensional strain accommodated between the eastern and western parts of the Alba Patera study area are attributable to the extensional strain localization along a few faults in the western part. These faults (on the left side in Fig. 2(c), labeled 15A through 15L) are deeper, with larger throws, and therefore accommodate more extensional strain than those in the eastern

Fig. 12. Compilation and comparison of D_{max}–L data for Martian and terrestrial normal faults. Linear trends on the diagrams indicate faults growing self-similarly, with constant aspect or length ratios, whereas curved trends indicate increasing values of aspect or length ratio as fault length increases. (a) Comparison of values for faults in the northern plains and Alba Patera study areas; filled triangles are from plateaued graben 16 in the eastern part of the study area. Curves to northern plains faults suggest vertical restriction at depths of 2–3 km (see text for discussion). (b) Comparison of normal faults from Earth and both Martian study areas; data for Italy and Greece from Roberts (2007) and plotted assuming average dip angles of 65° following Roberts and Michetti (2004). (c) Comparison of Martian fault sets and stratigraphically restricted normal faults from Fumanyá, Spain (data and curves from Soliva et al., 2005a,b).

part. Further, the larger faults clearly exploited smaller grabens as they grew, as apparent from their crosscutting relations and geometry. Interestingly, these faults produce stress shadows in the boundary element modeling such that it is difficult to simultaneously model the faults in close proximity to them. This implies that the assumption that all faults in the model are synchronous may not be appropriate to these faults. No evidence was found to support the generation of discrete stress shadows from the larger faults that might have inhibited nucleation and growth of smaller faults (see Ackermann and Schlische, 1997 for an example of stress shadowing), therefore the larger faults may have accommodated the large amount of extensional strain after formation of the smaller grabens such as those in the eastern domain. This relationship is consistent with the progressive evolution of normal fault populations in northeast Africa found by Soliva and Schultz (2008), with coalescense of distributed faults leading to the change from distributed to localized faulting.

6. Conclusions and implications

Measurements of fault-related topography along the Tantalus Fossae graben set reveal differences in displacement distribution and magnitude that imply spatial and possibly temporal variations in the extensional strain and displacement–length scaling relations recorded by Martian grabens. Using a complementary suite of techniques, including measured fault topography, mechanical modeling of fault displacements, and three-dimensional displacement–scaling relations, we suggest that grabens in the northern plains resulted from extensional deformation of a crustal section 2–3 km thick that may correspond to the thickness of sedimentary cover in this area. Closer to the center of Tharsis on Alba Patera, a similar set of grabens occurs to the east of a set of larger coalesced grabens that exhibit much larger displacements, extensional strains, and displacement–length ratios; these fault sets are consistent with deformation of a thick stack of volcanic flows. The different fault characteristics from north to south reveal this change in Martian stratigraphy in the northern Tharsis region. Based on morphologic expression and forward mechanical models, it appears that the larger structures may be a manifestation of progressive strain localization through time on Alba Patera. These results are consistent with the framework of deformation progression found by Cailleau et al. (2003). Quantitative examination of the spacing (e.g. Soliva et al., 2006), D_{max}–L ratios (e.g. Soliva and Benedicto, 2005), relay–ramp dimensions (e.g. Soliva and Benedicto, 2004), and length–frequency data (e.g. Gupta and Scholz, 2000b; Soliva and Schultz, 2008) holds promise for evaluating whether grabens from this or any area on Mars are restricted at depth.

Our results suggest a temporal transition from vertical restriction of uniformly spaced grabens to downward propagation and attendant widening of a few grabens, with an associated decrease in fault length ratio and increases in both D_{max}–L ratios and extensional strain. The evidence for a transition from linear to nonlinear D_{max}–L scaling in the northern plains compares favorably to examples of fault restriction identified on Earth (e.g. Soliva et al., 2005a,b, 2006; Soliva and Schultz, 2008). Fault growth in this part of Mars may then follow a stair-step trajectory involving early proportional growth and linear D_{max}–L scaling, followed by fault restriction, a faster rate of fault lengthening than displacement accumulation, and nonlinear D_{max}–L scaling (e.g. Cartwright et al., 1995; Schultz and Fossen, 2002; Soliva et al., 2005a,b). The normal faults in the western part of the Alba Patera study area may indicate reestablishment of proportional fault growth associated with down-dip propagation of the faults through a restricting horizon. The correlation of larger D_{max}–L ratios with larger extensional strain in the Alba Patera study area in conjunction with the results from the northern plains study area implies that mechanical stratigraphy and extensional strain might lead to different fault population characteristics in terms of fault spacing and individual fault size (length, depth, displacement) on Mars.

Acknowledgements

We thank Scott Marshall and an anonymous reviewer for their detailed and helpful comments that improved the final paper. Jaak Daemen and Steve Wesnousky provided thoughtful comments on an early version of this work. Thanks to Gerald Roberts for providing and discussing the normal fault data for Italy and Greece. This work was supported by NASA's Mars Data Analysis Program.

References

Ackermann, R.V., Schlische, R.W., 1997. Anticlustering of small normal faults around larger faults. Geology 25, 1127–1130.
Ackermann, R.V., Schlische, R.W., Withjack, M.O., 2001. The geometric and statistical evolution of normal fault systems: an experimental study of the effects of mechanical layer thickness on scaling laws. Journal of Structural Geology 23, 1803–1819.
Anderson, R.C., Dohm, J.M., Golombek, M.P., Haldemann, A.F.C., Franklin, B.J., Tanaka, K.L., Lias, J., Peer, B., 2001. Primary centers and secondary concentrations of tectonic activity through time in the western hemisphere of Mars. Journal of Geophysical Research 106, 20563–20585.
Banerdt, W.B., Golombek, M.P., Tanaka, K.L., 1992. Stress and tectonics on Mars. In: Kieffer, H.H., Jakosky, B.M., Snyder, C.W., Matthews, M.S. (Eds.), Mars. The University of Arizona Press, Tucson, pp. 249–297.
Benedicto, A., Schultz, R.A., Soliva, R., 2003. Layer thickness and the shape of faults. Geophysical Research Letters 30, 2076. doi:10.1029/2003GL018237.
Bohnenstiehl, D.R., Kleinrock, M.C., 1999. Faulting and fault scaling on the median valley floor of the trans-Atlantic geotraverse (TAG) segment, ~26°N on the mid-Atlantic ridge. Journal of Geophysical Research 104, 29351–29364.
Cailleau, B., Walter, T.R., Janle, P., Hauber, E., 2003. Modeling volcanic deformation in a regional stress field: implications for the formation of graben structures on Alba Patera, Mars. Journal of Geophysical Research 108, 5141. doi:10.1029/2003JE002135.
Cailleau, B., Walter, R.R., Janle, P., Hauber, E., 2005. Unveiling the origin of radial grabens on Alba Patera volcano by finite element modeling. Icarus 176, 44–56.
Carbotte, S.M., Macdonald, K.C., 1994. Comparison of seafloor tectonic fabric at intermediate, fast, and super fast spreading ridges: influence of spreading rate, plate motions, and ridge segmentation on fault patterns. Journal of Geophysical Research 99, 13609–13631.
Carr, M.H., 1974. Tectonism and volcanism of the Tharsis region of Mars. Journal of Geophysical Research 79, 3943–3949.
Cartwright, J.A., Trudgill, B.D., Mansfield, C.S., 1995. Fault growth by segment linkage: an explanation for scatter in maximum displacement and trace length data from the Canyonlands grabens of SE Utah. Journal of Structural Geology 17, 1319–1326.
Christensen, P.R., Bandfield, J.L., Smith, M.D., Hamilton, V.E., Clark, R.N., 2000. Identification of a basaltic component on the Martian surface from thermal emission spectrometer data. Journal of Geophysical Research 105, 9609–9621.
Clark, R.M., Cox, S.J.D., 1996. A modern regression approach to determining fault displacement–length relationships. Journal of Structural Geology 18, 147–152.
Cowie, P.A., Scholz, C.H., 1992a. Physical explanation for the displacement–length relationship of faults using a post-yield fracture mechanics model. Journal of Structural Geology 14, 1133–1148.
Cowie, P.A., Scholz, C.H., 1992b. Displacement–length scaling relationships for faults: data synthesis and discussion. Journal of Structural Geology 14, 1149–1156.
Cowie, P.A., Scholz, C.H., Edwards, M., Malinverno, A., 1993. Fault strain and seismic coupling on mid-ocean ridges. Journal of Geophysical Research 98, 17911–17920.
Crider, J.G., Pollard, D.D., 1998. Fault linkage: three-dimensional mechanical interaction between echelon normal faults. Journal of Geophysical Research 103, 24373–24391.
Crouch, S.L., 1976. Solution of plane elasticity problems by the displacement discontinuity method. International Journal of Numerical Methods 10, 301–343.
Crouch, S.L., Starfield, A.M., 1983. Boundary Element Methods in Solid Mechanics. Unwin Hyman Inc., Boston, 322 pp.
Davies, R.K., Crawford, M., Dula Jr., W.F., Cole, M.J., Dorn, G.A., 1997. Outcrop interpretation of seismic-scale normal faults in southern Oregon: description of structural styles and evaluation of subsurface interpretation methods. Leading Edge 16, 1135–1141.
Dawers, N.H., Anders, M.H., Scholz, C.H., 1993. Growth of normal faults: displacement–length scaling. Geology 21, 1107–1110.
Dawers, N.H., Anders, M.H., 1995. Displacement–length scaling and fault linkage. Journal of Structural Geology 17, 607–614.
Ernst, R.E., Grosfils, E.B., Mège, D., 2001. Giant dike swarms: Earth, Venus, and Mars. Annual Review of Earth and Planetary Sciences 29, 489–534.

Frey, H.V., Roark, J.H., Shockey, K.M., Frey, E.L., Sakimoto, S.E.H., 2002. Ancient lowlands on Mars. Geophysical Research Letters 29, 1384. doi:10.1029/2001GL013832.
Golombek, M.P., Phillips, R.J. Mars tectonics. In: Watters, T.R., Schultz, R.A. (Eds.), Planetary Tectonics. Cambridge University Press, Cambridge, in press.
Gross, M.R., Gutierrez-Alonso, G., Bai, T., Wacker, M.A., Collinsworth, K.B., Behl, R.J., 1997. Influence of mechanical stratigraphy and kinematics on fault scaling relations. Journal of Structural Geology 19, 171–183.
Gupta, A., Scholz, C.H., 2000a. A model of normal fault interaction based on observations and theory. Journal of Structural Geology 22, 865–879.
Gupta, A., Scholz, C.H., 2000b. Brittle strain regime transition in the Afar depression: implications for fault growth and seafloor spreading. Geology 28, 1078–1090.
Hamilton, V.E., Wyatt, M.B., McSween Jr., H.Y., Christensen, P.R., 2001. Analysis of terrestrial and Martian volcanic compositions using thermal emission spectroscopy. Journal of Geophysical Research 106, 14733–14746.
Hartmann, W.K., Neukum, G., 2001. Cratering chronology and the evolution of Mars. In: Chronology and Evolution of Mars. Kluwer Academic Publishers, Netherlands, pp. 165–194.
Kattenhorn, S.A., Pollard, D.D., 2001. Integrating 3D seismic data, field analogs and mechanical models in the analysis of segmented normal faults in the Wytch Farm oil field, southern England. AAPG Bulletin 85, 1183–1210.
Knapmeyer, M., Oberst, J., Hauber, E., Wählisch, M., Deuchler, C., Wagner, R., 2006. Working models for spatial distribution and level of Mars' seismicity. Journal of Geophysical Research 111, E11006. doi:10.1029/2006JE002708.
Martel, S.J., 2004. Mechanics of landslide initiation as a shear fracture phenomenon. Marine Geology 203, 319–339.
Mège, D., Masson, P., 1996. A plume tectonics model for the Tharsis province, Mars. Planetary Space Science 44, 1499–1546.
Nicol, A., Watterson, J., Walsh, J.J., Childs, C., 1996. The shapes, major axis orientations and displacement patterns of fault surfaces. Journal of Structural Geology 18, 235–248.
Okubo, C.H., Schultz, R.A., Stefanelli, G.S., 2004. Gridding Mars Orbiter Laser Altimeter data with GMT: effects of pixel size and interpolation methods on DEM integrity. Computers and Geosciences 30, 59–72.
Okubo, C.H., Schultz, R.A., 2004. Mechanical stratigraphy in the western equatorial region of Mars based on thrust fault-related fold topography and implications for near-surface volatile reservoirs. Geological Society of America Bulletin 116, 594–605.
Peacock, D.C.P., 1991. Displacements and segment linkage in strike-slip-fault zones. Journal of Structural Geology 13, 1025–1035.
Peacock, D.C.P., Sanderson, D.J., 1991. Displacements, segment linkage and relay ramps in normal-fault zones. Journal of Structural Geology 13, 721–734.
Peacock, D.C.P., Sanderson, D.J., 1994. Geometry and development of relay ramps in normal-fault systems. American Association of Petroleum Geologists Bulletin 78, 147–165.
Phillips, R.J., Zuber, M.T., Solomon, S.C., Golombek, M.P., Jakosky, B.M., Banerdt, W.B., Smith, D.E., Williams, R.M.E., Hynek, B.M., Aharonson, O., Hauck II, S.A., 2001. Ancient geodynamics and global-scale hydrology on Mars. Science 291, 2587–2591.
Plescia, J.B., Saunders, R.S., 1982. Tectonic history of the Tharsis region, Mars. Journal of Geophysical Research 87, 9775–9791.
Polit, A.T., 2005. Influence of Mechanical Stratigraphy and Strain on the Displacement–Length Scaling of Normal Faults on Mars. M.S. thesis, University of Nevada, Reno.
Poulimenos, G., 2000. Scaling properties of normal fault populations in the western Corinth graben, Greece: implications for fault growth in large strain settings. Journal of Structural Geology 22, 307–322.
Roark, J.H., Frey, H.V., 2001. Gridview: recent improvements in research and education software for exploring Mars topography. Lunar and Planetary Science Conference 32 (abstract 1618).
Roberts, G.P., 2007. Fault orientation variations along the strike of active normal fault systems in Italy and Greece: implications for predicting the orientations of subseismic-resolution faults in hydrocarbon reservoirs. AAPG Bulletin 91, 1–20.
Roberts, G.P., Michetti, A.-M., 2004. Spatial and temporal variations in growth rates along active normal fault systems: an example from the Lazio–Abruzzo Apennines, central Italy. Journal of Structural Geology 26, 339–376.
Schlische, R.W., Young, S.S., Ackermann, R.V., Gupta, A., 1996. Geometry and scaling relations of a population of very small rift related normal faults. Geology 24, 683–686.
Scholz, C.H., 1997. Earthquake and fault populations and the calculation of brittle strain. Geowissenschaften 15, 124–130.
Scholz, C.H., 2002. The Mechanics of Earthquakes and Faulting, second ed. Cambridge University Press, 471 pp.
Scholz, C.H., Cowie, P.A., 1990. Determination of total strain from faulting using slip measurements. Nature 346, 837–838.
Scholz, C.H., Dawers, N.H., Yu, J.Z., Anders, M.H., Cowie, P.A., 1993. Fault growth and fault scaling laws – preliminary results. Journal of Geophysical Research 98, 21951–21961.
Schultz, R.A., 1992. Mechanics of curved slip surfaces in rock. Engineering Analysis with Boundary Elements 10, 147–154.
Schultz, R.A., 1995. Limits on strength and deformation properties of jointed basaltic rock masses. Rock Mechanics and Rock Engineering 28, 1–15.
Schultz, R.A., 1996. Relative scale and the strength and deformability of rock masses. Journal of Structural Geology 18, 1139–1149.
Schultz, R.A., 1999. Understanding the process of faulting: selected challenges and opportunities at the edge of the 21st century. Journal of Structural Geology 21, 985–993.
Schultz, R.A., 2003. A method to relate initial elastic stress to fault population strains. Geophysical Research Letters 30, 1593. doi:10.1029/2002GL016681.
Schultz, R.A., Aydin, A., 1990. Formation of interior basins associated with curved faults in Alaska. Tectonics 9, 1387–1407.
Schultz, R.A., Fossen, H., 2002. Displacement–length scaling in three dimensions: the importance of aspect ratio and application to deformation bands. Journal of Structural Geology 24, 1389–1411.
Schultz, R.A., Lin, J., 2001. Three-dimensional normal faulting models of Valles Marineris, Mars, and geodynamic implications. Journal of Geophysical Research 106, 16549–16566.
Schultz, R.A., Okubo, C.H., Wilkins, S.J., 2006. Displacement–length scaling relations for faults on the terrestrial planets. Journal of Structural Geology 28, 2182–2193.
Schultz, R.A., Soliva, R., Fossen, H., Okubo, C.H., Reeves, D.M., 2008. Dependence of displacement–length scaling relations for fractures and deformation bands on the volumetric changes across them. Journal of Structural Geology 30, 1405–1411.
Schultz, R.A., Soliva, R., Okubo, C.H., Mège, D. Fault populations. In: Watters, T.R., Schultz, R.A. (Eds.), Planetary Tectonics. Cambridge University Press, Cambridge, in press.
Scott, D.H., Tanaka, K.L., 1986. Geologic map of the western equatorial region of Mars. United States Geological Survey Map I-1802-A, scale 1:15,000,000.
Smith, D.E., Zuber, M.T., Frey, H.V., Garvin, J.B., Head, J.W., Muhleman, D.O., Pettengill, G.H., Phillips, R.J., Solomon, S.C., Zwally, H.J., Banderdt, W.B., Duxbury, T.C., Golombek, M.P., Lemoine, F.G., Neumann, G.A., Rowlands, D.D., Aharonson, O., Ford, P.G., Ivanov, A.B., Johnson, C.L., McGovern, P.J., Abshire, J.B., Afzal, R.S., Sun, X., 2001. Mars Orbiter Laser Altimeter: experiment summary after the first year of global mapping of Mars. Journal of Geophysical Research 106 (E10), 23689–23722.
Soliva, R., Benedicto, A., 2004. A linkage criterion for segmented normal faults. Journal of Structural Geology 26, 2251–2267.
Soliva, R., Benedicto, A., 2005. Geometry, scaling relations and spacing of vertically restricted normal faults. Journal of Structural Geology 27, 317–325.
Soliva, R., Benedicto, A., Vergély, P., Rives, T., 2005a. Mechanical control of a lithological alternation on normal fault morphology, growth and reactivation. Bulletin de la Société Géologique de France 176 (4), 329–342.
Soliva, R., Schultz, R.A., Benedicto, A., 2005b. Three-dimensional displacement–length scaling and maximum dimension of normal faults in layered rocks. Geophysical Research Letters 32, L16302. doi:10.1029/2005GL023007.
Soliva, R., Benedicto, A., Maerten, L., 2006. Spacing and linkage of confined normal faults: importance of mechanical thickness. Journal of Geophysical Research 111, B01402. doi:10.1029/2004JB003507.
Soliva, R., Benedicto, A., Schultz, R.A., Maerten, L., Micarelli, L., 2008. Displacement and interaction of normal fault segments branched at depth: implications for fault growth and potential earthquake rupture size. Journal of Structural Geology 30, 1288–1299.
Soliva, R., Schultz, R.A., 2008. Distributed and localized faulting in extensional settings: insight from the North Ethiopian rift – Afar transition area. Tectonics 27, TC2003. doi:10.1029/2007TC002148.
Solomon, S.C., Head, J.W., 1982. Evolution of the Tharsis province of Mars: the importance of heterogeneous lithospheric thickness and volcanic construction. Journal of Geophysical Research 87, 9755–9774.
Spyropoulos, C., Griffith, W.J., Scholz, C.H., Shaw, B.E., 1999. Experimental evidence for different strain regimes of crack populations in a clay model. Geophysical Research Letters 26, 1081–1084.
Tanaka, K.L., 1990. Tectonic history of the Alba Patera–Ceraunius Fossae region of Mars. Proceedings of Lunar and Planetary Science Conference 20, 515–523.
Tanaka, K.L., Skinner Jr., J.A., Hare, T.M., Joyal, T., Wenker, A., 2003. Resurfacing history of the northern plains of Mars based on geologic mapping of Mars Global Surveyor Data. Journal of Geophysical Research 108 (E4), 8043. doi:10.1029/2002JE001908.
Villemin, T., Angelier, J., Sunwoo, C., 1995. Fractal distribution of fault length and offsets: implications of brittle deformation evaluation – the Lorrain coal basin. In: Barton, C.C., LaPointe, P.R. (Eds.), Fractals in the Earth Sciences. Plenum Press, New York, pp. 205–225.
Wilkins, S.J., Gross, M.R., 2002. Normal fault growth in layered rocks at Split Mountain, Utah. Journal of Structural Geology 24, 1413–1429.
Wilkins, S.J., Schultz, R.A., Anderson, R.C., Dohm, J.M., Dawers, N.H., 2002. Deformation rates from faulting at the Tempe Terra extensional province. Mars. Geophysical Research Letters 29, 1884. doi:10.1029/2002GL015391.
Willemse, E.J.M., 1997. Segmented normal faults: correspondence between three-dimensional mechanical models and field data. Journal of Geophysical Research 102, 675–692.
Willemse, E.J.M., Pollard, D.D., Aydin, A., 1996. Three-dimensional analyses of slip distributions on normal fault arrays with consequences for fault scaling. Journal of Structural Geology 18, 295–309.
Williams, J.P., Nimmo, F., Moore, W.B., Paige, D.A., 2008. The formation of Tharsis on Mars: what the line-of-sight gravity is telling us. Journal of Geophysical Research 113, E10011. doi:10.1029/JE003050.
Zuber, M.T., Solomon, S.C., Phillips, R.J., Smith, D.E., Tyler, G.L., Aharonson, O., Balmino, G., Banderdt, W.B., Head, J.W., Johnson, C.L., Lemoine, F.G., McGovern, P.J., Neumann, G.A., Rowlands, D.D., Zhong, S., 2000. Internal structure and early thermal evolution of Mars from Mars Global Surveyor topography and gravity. Science 287, 1788–1793.